

# Cesium Phosphotungstate Salt Nanospheres Coated on a 3D Graphene Framework for Lithium Ion Batteries

Mengyao Wang<sup>+[a]</sup>, Guang Yang<sup>+[a]</sup>, Chunyu Sun,<sup>[a]</sup> Yuchao Wu,<sup>[a]</sup> Xinyuan Jiang,<sup>[a]</sup> Lubin Ni,<sup>\*[a]</sup> Guowang Diao,<sup>\*[a]</sup> and Yongge Wei<sup>\*[b]</sup>

Traditional cathode materials for lithium-insertion compounds, such as  $\text{LiCoO}_2$ ,  $\text{LiMn}_2\text{O}_4$ ,  $\text{LiNiO}_2$ , and  $\text{LiFePO}_4$ , have been highly successful, but they face severe limitations in terms of energy density and production cost associated with their usage. Therefore, the design of next-generation energy storage devices, such as molecular cluster batteries, is an important and hot topic in current research. While polyoxometalates have been developed for battery components for several years, common POMs, including  $\text{H}_3\text{PW}_{12}\text{O}_{40}$ , tend to form heteropoly blues that dissolve in the electrolyte during charging and discharging processes. Hence, finding a polyoxometalates that is less soluble in electrolyte and exhibits certain electrical properties is particularly crucial for lithium-ion battery cathodes.

Here, we report the synthesis of zero-dimensional  $\text{Cs}_3\text{PW}_{12}\text{O}_{40}$  nanospheres, followed by the successful embedding of  $\text{Cs}_3\text{PW}_{12}\text{O}_{40}$  nanospheres into three-dimensional graphene sponge, constructing a novel hybrid material of three-dimensional graphene@polyoxometalate ( $\text{rGO}@\text{Cs}_3\text{PW}_{12}\text{O}_{40}$ ) as a new cathode material for LIBs. The prepared  $\text{rGO}@\text{Cs}_3\text{PW}_{12}\text{O}_{40}$  half-cell hybrid exhibits excellent electrochemical performance, with high specific capacity (approximately  $240 \text{ mAh g}^{-1}$  at  $50 \text{ mA g}^{-1}$ ), outstanding rate capability ( $95 \text{ mAh g}^{-1}$  at  $2 \text{ A g}^{-1}$ ), and exceptional cycling stability (700 cycles at  $1 \text{ A g}^{-1}$ ). This study provides a new perspective on the application of polyoxometalates in lithium-ion batteries.

## Introduction

Lithium-ion batteries represent a pivotal advancement in electrochemical energy storage systems. These cells have not only enhanced the efficiency and convenience of daily energy utilization but have also catalyzed advancements in sectors including electric mobility, grid-scale renewable integration, and unmanned aerial vehicles.<sup>[1]</sup> The heightened interest in lithium-ion technology can be attributed to its superior gravimetric and volumetric energy densities.<sup>[2]</sup> This translates to the ability to store a considerable quantum of electrical energy in a constrained form factor, solidifying their role as a primary energy reservoir in various applications.<sup>[3]</sup> Despite the widespread and long-term applications of lithium-ion batteries (LIBs), numerous challenges remain in achieving high performance, safety, and cost-effectiveness. For instance, the high cost, toxic nature, low theoretical capacity, and safety concerns associated with layered  $\text{LiCoO}_2$  materials significantly hinder

their further practical application in large-scale LIBs.<sup>[4]</sup> Spinel  $\text{LiMn}_2\text{O}_4$ , while a promising candidate, exhibits severe capacity degradation during long-term electrochemical cycling, particularly at elevated temperatures. This degradation is primarily due to the dissolution of  $\text{Mn}^{2+}$  ions into the electrolyte, electrolyte decomposition under high pressure, and structural deformation induced by the Jahn-Teller effect of  $\text{Mn}^{3+}$  ions.<sup>[5]</sup> Furthermore, although olivine-type  $\text{LiFePO}_4$  materials have recently found use in electric vehicles and energy storage systems, the inherent low electronic conductivity and limited rate performance of  $\text{LiFePO}_4$  restrict its overall electrochemical performance and widespread commercialization. Consequently, there is an urgent need for the development of novel cathode materials capable of rich, reversible multi-electron redox reactions and fast lithium-ion diffusion to meet the increasing demands for high-capacity batteries with rapid charge/discharge capabilities.<sup>[6]</sup> Polyoxometalates (POMs),<sup>[7]</sup> a class of single-molecule clusters characterized by diverse structures, rich functionality, and a wide range of topological structures and chemical compositions. It exhibits excellent properties and extensive applications in energy-related devices,<sup>[7]</sup> catalysis,<sup>[8]</sup> electrochemistry,<sup>[9]</sup> energy storage,<sup>[10]</sup> energy conversion,<sup>[11]</sup> photochemistry,<sup>[12]</sup> ion conductivity,<sup>[13]</sup> and electrochemical biosensors.<sup>[14]</sup> Therefore, utilizing its unique properties and structural features, achieving highly reversible multi-electron redox reactions and rapid lithium ion diffusion ability of polyoxometalate clusters has become one of the challenges.<sup>[15]</sup> During the charging and discharging process, POMs act as an "ion sponge" to promote the reversible absorption and release of charge carriers, and also serves as an "electron sponge" to enhance electrode reaction kinetics.<sup>[16]</sup> POMs represent a large class of metal oxygen clusters (usually Mo, W, V),<sup>[17]</sup> which are in

[a] M. Wang,<sup>+[a]</sup> G. Yang,<sup>+[a]</sup> C. Sun, Y. Wu, X. Jiang, Prof. L. Ni, Prof. G. Diao

School of Chemistry and Chemical Engineering

Yangzhou University School of Chemistry and Chemical Engineering,

Yangzhou University

Yangzhou, 225002 Jiangsu (P. R. China)

E-mail: Ibni@yzu.edu.cn

gwdiao@yzu.edu.cn

[b] Prof. Y. Wei

School of Key Lab of Organic Optoelectronics & Molecular Engineering of

Ministry of Education, Department of Chemistry, Tsinghua University

Beijing 100084 (P. R. China)

E-mail: yonggewei@tsinghua.edu.cn

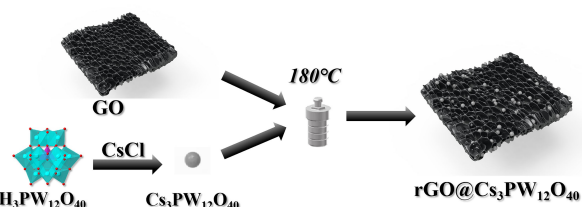
[+] These authors contributed equally

Supporting information for this article is available on the WWW under <https://doi.org/10.1002/batt.202400711>

the highest oxidation state, forming large closed molecular level 3D frameworks, with phosphotungstic acid being one of them.

Furthermore, we still need deeper insight the charge reaction mechanism of POMs-based electrodes to design effective solutions to solve the incomplete utilization of POMs, rapid degradation and poor Coulomb efficiency during charge and discharge. These limitations hinder its application as a cathode material in lithium-ion batteries. Hence, POMs converted,<sup>[18]</sup> combining with MOFs,<sup>[15,19]</sup> and hybridizing with graphene<sup>[20]</sup> are considered several alternative methods. In 2017, Ni et al. prepared 3D self-assembly rGO@PANI/PW<sub>12</sub> can provide a reversible charging and discharging capacity of 285 mAhg<sup>-1</sup> at a current density of 50 mA g<sup>-1</sup>.<sup>[21]</sup> A. Bayaguud et al. transformed POMs into three-dimensional porous lithium-containing oxides, exhibiting an excellent specific capacity of 198 mAhg<sup>-1</sup> at a current density of approximately 10 Ag<sup>-1</sup>.<sup>[18]</sup> X. Yang et al. synthesized the first nano cage based metal organic framework (Zn POMCF) containing polyoxometalates (POMs) using surface catalyst assisted methods, and demonstrated its high stability and good electrochemical performance in lithium-ion batteries (LIBs).<sup>[15]</sup> K. Wakamatsu et al. prepared POM/oxidized CNH (CNHox) hybrid materials with capacity retention at high current densities.<sup>[34]</sup> Research on the energy storage direction of POMs has gradually emerged due to their beautiful structure and electrochemical performance.<sup>[15–35]</sup> Based on the current literature, while numerous studies have focused on preventing the dissolution of polyoxometalates (POMs) in electrolytes, there has been limited attention given to investigating the solubility of the polyacids themselves.

In this work, we conducted relevant tests and found that the cesium phosphotungstate, synthesized by replacing phosphotungstic acid with cesium alkali metal cations, is indeed poorly soluble in the LiPF<sub>6</sub> electrolyte (Figure S2 in the Supporting Information). However, its conductivity is still very low and its insulation performance remains unchanged. To overcome this, a rGO@Cs<sub>3</sub>PW<sub>12</sub>O<sub>40</sub> hybrid material with good conductivity and relatively high specific surface area was developed in this work through the electrostatic interaction between graphene and cesium phosphotungstate (Scheme 1). After 700 cycles, its specific discharge capacity can still be maintained at around 105 mAh/g.



Scheme 1. Schematic diagram of rGO@Cs<sub>3</sub>PW<sub>12</sub>O<sub>40</sub> preparation.

## Results and Discussion

The morphology and microstructure of Cs<sub>3</sub>PW<sub>12</sub>O<sub>40</sub> and rGO@Cs<sub>3</sub>PW<sub>12</sub>O<sub>40</sub> were confirmed by using scanning electron and transmission electron microscopy (SEM and TEM) (Figure 1 and Figure 2). It can be observed from Figure 1a and Figure 1b that the morphology of Cs<sub>3</sub>PW<sub>12</sub>O<sub>40</sub> is solid spherical, and its particle size is roughly uniform, most of which are between 400 and 800 nm. The rGO@Cs<sub>3</sub>PW<sub>12</sub>O<sub>40</sub> is shown in Figure 1c and Figure 1d, in which Cs<sub>3</sub>PW<sub>12</sub>O<sub>40</sub> is uniformly distributed in the layered graphene pores, forming a three-dimensional sandwich

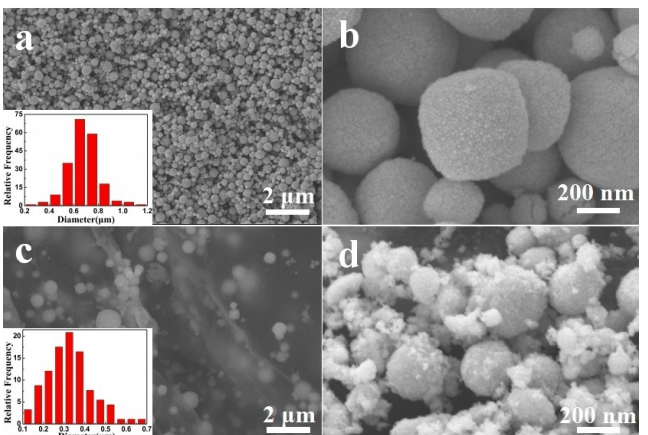


Figure 1. SEM of (a, b) Cs<sub>3</sub>PW<sub>12</sub>O<sub>40</sub>; (c, d) rGO@Cs<sub>3</sub>PW<sub>12</sub>O<sub>40</sub>.

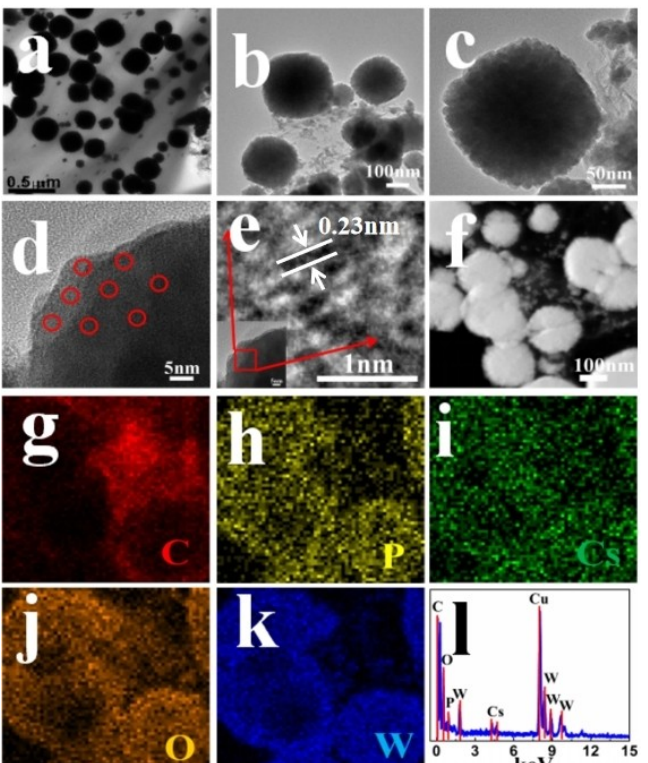
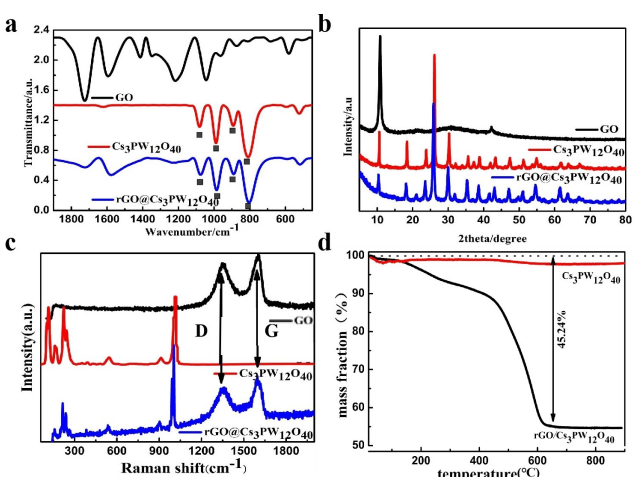


Figure 2. (a-c) TEM of rGO@Cs<sub>3</sub>PW<sub>12</sub>O<sub>40</sub>; (d,e) HR-TEM of rGO@Cs<sub>3</sub>PW<sub>12</sub>O<sub>40</sub>; (f-l) Dark field STEM and EDS elemental mapping images of rGO@Cs<sub>3</sub>PW<sub>12</sub>O<sub>40</sub>.

structure. In the figure, the particle size of  $\text{Cs}_3\text{PW}_{12}\text{O}_{40}$  has decreased, and most of them are in the range of 200~600 nm. This is due to the regrowth of  $\text{Cs}_3\text{PW}_{12}\text{O}_{40}$  molecules at high temperature during the hydrothermal synthesis process. Such the structure is conducive to preventing the agglomeration caused by the  $\pi$ - $\pi$  effect of graphene. The interlayer spacing of graphene increases the specific surface area of 3D sponge-loaded graphene so that more  $\text{Cs}_3\text{PW}_{12}\text{O}_{40}$  molecules are embedded in the pores of graphene, resulting in a stable structure of rGO@ $\text{Cs}_3\text{PW}_{12}\text{O}_{40}$  and excellent electrical conductivity. We verified that the prepared  $\text{Cs}_3\text{PW}_{12}\text{O}_{40}$  is not easily soluble in  $\text{LiPF}_6$  electrolyte (Figure S2 in the supporting information). The hybridization of rGO and  $\text{Cs}_3\text{PW}_{12}\text{O}_{40}$  further prevents dissolution, while increasing the conductivity of the material and providing an ion transport pathway.

From Figure 2a and 2b, the  $\text{Cs}_3\text{PW}_{12}\text{O}_{40}$  spheres in the rGO@ $\text{Cs}_3\text{PW}_{12}\text{O}_{40}$  hybrid material are uniformly dispersed in graphene, with uneven sizes. This structure is available for a large specific surface area, and its rough skeleton is easy to form a three-dimensional structure, which is conducive to providing positions for  $\text{Li}^+$  insertion and detachment, and is conducive to the transmission of electrons in electrochemical reactions. This greatly improves the conductivity and lithium storage capacity of the hybrid material. From Figure 2c, the morphology of  $\text{Cs}_3\text{PW}_{12}\text{O}_{40}$  is consistent with the morphology tested in Figure 2a and 2b, which is a rough solid spherical structure with a particle size between 200 and 600 nm. It also reveals that small particles of cesium phosphotungstate molecules are uniformly distributed in the  $\text{Cs}_3\text{PW}_{12}\text{O}_{40}$  microspheres through the corresponding HRTEM (Figure 2d and 2e), and the lattice spacing of  $\text{Cs}_3\text{PW}_{12}\text{O}_{40}$  molecules is approximately 0.23 nm through measurement. Figure 2f shows a STEM plot taken, and EDS spectroscopy tests were conducted on the positions for elements C, P, Cs, O and W (Figure 2g~2k). The spherical morphology of  $\text{Cs}_3\text{PW}_{12}\text{O}_{40}$  can be clearly observed from the elemental distribution of Cs, P, O, and W. The C element distribution indicates that  $\text{Cs}_3\text{PW}_{12}\text{O}_{40}$  is loaded on rGO. Figure 2l shows an EDS of rGO@ $\text{Cs}_3\text{PW}_{12}\text{O}_{40}$  hybrid material, further proving the presence of C, Cs, P, W, and O in rGO@ $\text{Cs}_3\text{PW}_{12}\text{O}_{40}$ . Figure S3 assists in proving this structure. The specific surface area reduced from  $129 \text{ m}^2 \text{ g}^{-1}$  to  $39 \text{ m}^2 \text{ g}^{-1}$ , indicating that  $\text{Cs}_3\text{PW}_{12}\text{O}_{40}$  was successfully coated with rGO. Due to the small pore size of  $\text{Cs}_3\text{PW}_{12}\text{O}_{40}$  nanospheres, there is minimal change in the pore size before and after composite formation, with the pore diameter decreasing from the original 7.314 nm to 3.152 nm. As shown in Figure S4, micropore analysis further confirms that the pore size is 3.949 nm, indicating the absence of smaller pores.

$\text{Cs}_3\text{PW}_{12}\text{O}_{40}$  and rGO@ $\text{Cs}_3\text{PW}_{12}\text{O}_{40}$  has been further characterized using a wide range of analytical methods. In the FTIR spectra (Figure 3a),  $\text{Cs}_3\text{PW}_{12}\text{O}_{40}$  has four groups of characteristic absorption peaks, namely 1084, 984, 891 and  $808 \text{ cm}^{-1}$ . These characteristic peak positions correspond to the bending vibration of  $\nu_{as}(\text{P}-\text{O}_a)$ , the antisymmetric stretching vibration of  $\nu_{as}(\text{W}-\text{O}_t)$ , and the stretching vibration absorption peaks of  $\nu_{as}(\text{W}-\text{O}_b-\text{W})$  and  $\nu_{as}(\text{W}-\text{O}_c-\text{W})$  in  $\text{Cs}_3\text{PW}_{12}\text{O}_{40}$ , respectively. When comparing  $\nu_{as}(\text{W}-\text{O}_t)$ , terminal  $\nu_{as}(\text{W}-\text{O}_t)$ , corner sharing



**Figure 3.** FT-IR spectra of GO,  $\text{Cs}_3\text{PW}_{12}\text{O}_{40}$  and rGO@ $\text{Cs}_3\text{PW}_{12}\text{O}_{40}$ ; (b) XRD patterns of GO,  $\text{Cs}_3\text{PW}_{12}\text{O}_{40}$  and rGO@ $\text{Cs}_3\text{PW}_{12}\text{O}_{40}$ ; (c) Raman spectra of GO,  $\text{Cs}_3\text{PW}_{12}\text{O}_{40}$  and rGO@ $\text{Cs}_3\text{PW}_{12}\text{O}_{40}$ ; (d) TGA curves of  $\text{Cs}_3\text{PW}_{12}\text{O}_{40}$  and rGO@ $\text{Cs}_3\text{PW}_{12}\text{O}_{40}$ .

$\nu_{as}(\text{W}-\text{O}_b-\text{W})$ , and edge sharing  $\nu_{as}(\text{W}-\text{O}_c-\text{W})$ , the changes in the positions of these four absorption vibration peaks in the rGO@ $\text{Cs}_3\text{PW}_{12}\text{O}_{40}$  indicate that the changes in electronic distribution and structural deformation of the composite material are due to the strong electrostatic interaction between rGO and  $\text{Cs}_3\text{PW}_{12}\text{O}_{40}$ .<sup>[37,38]</sup> In addition, the XRD patterns of hybrids rGO@ $\text{Cs}_3\text{PW}_{12}\text{O}_{40}$  and  $\text{Cs}_3\text{PW}_{12}\text{O}_{40}$  (Figure 3b) is shown obvious POM characteristic peaks, indicating that  $\text{Cs}_3\text{PW}_{12}\text{O}_{40}$  maintains structural integrity in hybridization.<sup>[37–40]</sup> In the Raman spectrum (Figure 3c), the GO curve exhibits two prominent peaks: the D band at  $1345 \text{ cm}^{-1}$  and the G band at  $1607 \text{ cm}^{-1}$ . In the hybrid rGO@ $\text{Cs}_3\text{PW}_{12}\text{O}_{40}$ , the  $I_D/I_G$  ratio increases from 0.78 in the GO spectrum to 0.85, suggesting a higher degree of internal disorder, an increase in defects, and further reduction of graphene.<sup>[21]</sup> Additionally, a distinct peak corresponding to  $\text{Cs}_3\text{PW}_{12}\text{O}_{40}$  is observed, indicating that the nanospheres are fully incorporated into the reduced graphene oxide. Thermogravimetric analysis (TGA) measurements (Figure 3d) are usually performed to determine the composition of  $\text{Cs}_3\text{PW}_{12}\text{O}_{40}$ , and hybrids rGO@ $\text{Cs}_3\text{PW}_{12}\text{O}_{40}$ . The  $\text{Cs}_3\text{PW}_{12}\text{O}_{40}$  hybrid material exhibited minimal capacity loss when calcined up to  $900^\circ\text{C}$ , with only 1.5% of the bound water mass lost within the temperature range of 25–60 °C. In the case of rGO@ $\text{Cs}_3\text{PW}_{12}\text{O}_{40}$ , 7.4% of the bound water was lost within the temperature range of 25–280 °C, while the carbon component in graphene was released as  $\text{CO}_2$  between 280–600 °C, resulting in an approximate 37.84% carbon loss. Consequently, about 54.76% of  $\text{Cs}_3\text{PW}_{12}\text{O}_{40}$  remained.

To verify its mechanism of action in lithium-ion batteries, we conducted a study on the performance of lithium-ion batteries using rGO@ $\text{Cs}_3\text{PW}_{12}\text{O}_{40}$  as the cathode and  $\text{Cs}_3\text{PW}_{12}\text{O}_{40}$  as a comparison sample. Rate performance of  $\text{Cs}_3\text{PW}_{12}\text{O}_{40}$ , rGO@ $\text{Cs}_3\text{PW}_{12}\text{O}_{40}$  cathodes at different current densities, ranging from  $50 \text{ mA g}^{-1}$  to  $2 \text{ A g}^{-1}$  are shown in Figure 4a. At current densities of  $50 \text{ mA g}^{-1}$ ,  $100 \text{ mA g}^{-1}$ ,  $200 \text{ mA g}^{-1}$ ,  $500 \text{ mA g}^{-1}$ ,  $1 \text{ A g}^{-1}$ ,  $2 \text{ A g}^{-1}$ , and  $50 \text{ mA g}^{-1}$ , the corresponding

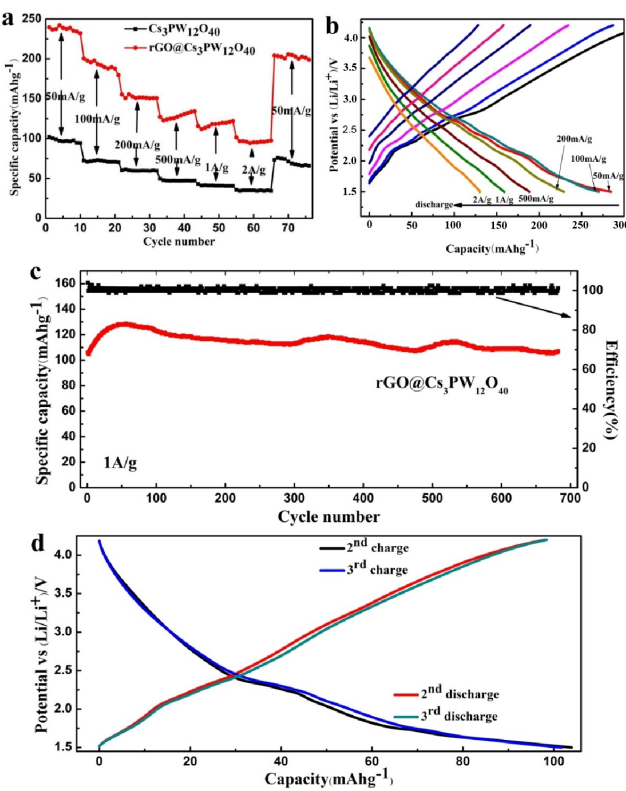


**Figure 4.** (a) Rate performance of  $\text{Cs}_3\text{PW}_{12}\text{O}_{40}$ , rGO@ $\text{Cs}_3\text{PW}_{12}\text{O}_{40}$  cathodes at different current densities, ranging from  $50 \text{ mA g}^{-1}$  to  $2 \text{ A g}^{-1}$ ; (b) The second galvanostatic charge-discharge profiles for rGO@ $\text{Cs}_3\text{PW}_{12}\text{O}_{40}$  over the voltage range of  $1.5$ – $4.2$  V versus  $\text{Li}^+/\text{Li}$  at various current densities, collected from different cells. (c) Long-term cycling performance of rGO@ $\text{Cs}_3\text{PW}_{12}\text{O}_{40}$ .

rGO@ $\text{Cs}_3\text{PW}_{12}\text{O}_{40}$  discharge specific capacities are  $240 \text{ mAh g}^{-1}$ ,  $195 \text{ mAh g}^{-1}$ ,  $155 \text{ mAh g}^{-1}$ ,  $125 \text{ mAh g}^{-1}$ ,  $115 \text{ mAh g}^{-1}$ ,  $95 \text{ mAh g}^{-1}$ ,  $205 \text{ mAh g}^{-1}$ , respectively. The discharge specific capacities of lithium-ion batteries prepared with  $\text{Cs}_3\text{PW}_{12}\text{O}_{40}$  hybrid material are  $105 \text{ mAh g}^{-1}$ ,  $75 \text{ mAh g}^{-1}$ ,  $60 \text{ mAh g}^{-1}$ ,  $48 \text{ mAh g}^{-1}$ ,  $40 \text{ mAh g}^{-1}$ ,  $35 \text{ mAh g}^{-1}$ ,  $73 \text{ mAh g}^{-1}$ . Through data analysis and comparison, it is demonstrated that after multiple cycles, lithium ion batteries prepared from rGO@ $\text{Cs}_3\text{PW}_{12}\text{O}_{40}$  hybrid material have good cycling performance in terms of discharge specific capacity, and can quickly charge and discharge with high current, with minimal capacity loss. Figure 4c shows the performance chart of the charge discharge cycle of a lithium-ion battery prepared from rGO@ $\text{Cs}_3\text{PW}_{12}\text{O}_{40}$  hybrid material at a current density of  $1 \text{ A g}^{-1}$  for 700 cycles shows that its discharge specific capacity is relatively small at the beginning, only  $103 \text{ mAh g}^{-1}$ , and then continues to increase until the 50th cycle. The discharge specific capacity reaches the maximum value of  $128 \text{ mAh g}^{-1}$  at the 50th cycle, gradually decreasing, but gradually maintaining at  $110 \text{ mAh g}^{-1}$ . There is a small increase and decrease at the 300–350 cycles, and finally reaching 700 cycles, its discharge specific capacity can still be maintained at around  $105 \text{ mAh g}^{-1}$ , indicating that the cycling performance of lithium-ion batteries prepared from rGO@ $\text{Cs}_3\text{PW}_{12}\text{O}_{40}$  hybrid material is relatively stable. Figure 4d shows the first two cycles of charge and discharge performance of lithium-ion batteries prepared from rGO@ $\text{Cs}_3\text{PW}_{12}\text{O}_{40}$  hybrid

material at a current density of  $1 \text{ A g}^{-1}$  after 700 cycles show four good redox fluctuations:  $2.38$ ,  $2.21$ ,  $2.06$ , and  $1.65$  ( $\text{Li}/\text{Li}^+$ ) V during the charge and discharge processes of  $4.2$ – $1.5$  ( $\text{Li}/\text{Li}^+$ ) V. This reflects the excellent reversible ability of rGO@ $\text{Cs}_3\text{PW}_{12}\text{O}_{40}$  hybrid material. The rGO@ $\text{Cs}_3\text{PW}_{12}\text{O}_{40}$  hybrid material has a good ( $103 \text{ mAh g}^{-1}$ ) capacity in the second cycle of charge and discharge, but it is lower than its theoretical capacity ( $223 \text{ mAh g}^{-1}$ ). This is because the reaction of tungsten in the battery may involve transitions from different oxidation states such as  $+6$ ,  $+5$ ,  $+4$ , which can affect the energy storage capacity of phosphotungstic acid.<sup>[42]</sup>

Cyclic voltammograms (CVs) of rGO@ $\text{Cs}_3\text{PW}_{12}\text{O}_{40}$  electrode for the first two cycles at a scan rate of  $0.1 \text{ mV s}^{-1}$  in the potential range of  $1.5$ – $4.2$  V are shown in Figure 5a. Due to the oxidation-reduction reaction between  $\text{W}^{6+}$  and  $\text{W}^{4+}$  ions in  $\text{Cs}_3\text{PW}_{12}\text{O}_{40}$ , there are three pairs of oxidation-reduction values during its charging and discharging, namely  $2.42/2.25$ ,  $2.16/2.02$ , and  $1.80/1.63$  ( $\text{Li}/\text{Li}^+$ ) V. Therefore, the insertion and removal of lithium ions in rGO@ $\text{Cs}_3\text{PW}_{12}\text{O}_{40}$  hybrid material is a multi-step process. Simultaneously indicating that a reversible electrochemical reaction occurs between the rGO@ $\text{Cs}_3\text{PW}_{12}\text{O}_{40}$  hybrid material and the lithium anode.  $\text{Cs}_3\text{PW}_{12}\text{O}_{40}$  is an “electron sponge” that charges and discharges within the potential range of  $4.2$ – $1.5$  ( $\text{Li}/\text{Li}^+$ ) V. In order to better analyze the advantages of rGO@ $\text{Cs}_3\text{PW}_{12}\text{O}_{40}$ , Electrochemical impedance spectroscopy (EIS) measurements of rGO@ $\text{Cs}_3\text{PW}_{12}\text{O}_{40}$  hybrid and  $\text{Cs}_3\text{PW}_{12}\text{O}_{40}$  as cathode material for lithium-ion batteries are conducted. The Nyquist results are shown in Figure 5b, the Nyquist plot of rGO@ $\text{Cs}_3\text{PW}_{12}\text{O}_{40}$  hybrid electrode and  $\text{Cs}_3\text{PW}_{12}\text{O}_{40}$  electrode spreads a concave semicircle curve in the high-frequency region and a diagonal line in the low-frequency region. In the medium to high frequency range, the semicircle radius of rGO@ $\text{Cs}_3\text{PW}_{12}\text{O}_{40}$  hybrid electrode is smaller than that of pure  $\text{Cs}_3\text{PW}_{12}\text{O}_{40}$  electrode, indicating that the contact resistance and charge transfer impedance of rGO@ $\text{Cs}_3\text{PW}_{12}\text{O}_{40}$  hybrid electrodes are relatively small. The equivalent circuit model used in this research system shows possible impedances during testing, including electrolyte impedance ( $R_e$ ), contact impedance ( $R_f$ ), charge transfer impedance ( $R_{ct}$ ), and lithium ion diffusion impedance ( $Z_w$ ). The contact impedance ( $R_f$ ) and charge transfer impedance ( $R_{ct}$ ) of rGO@ $\text{Cs}_3\text{PW}_{12}\text{O}_{40}$  used as cathodes for lithium-ion batteries are  $101.2 \Omega$  and  $17.5 \Omega$ , respectively, which are much smaller than the  $174.4 \Omega$  and

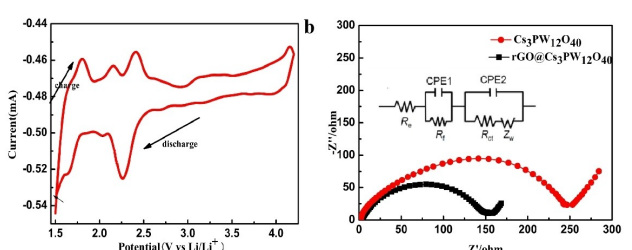


**Figure 5.** (a) Cyclic voltammetry curves of rGO@ $\text{Cs}_3\text{PW}_{12}\text{O}_{40}$  electrode swept in the voltage range of  $1.5$ – $4.2$  V at a sweep rate of  $0.1 \text{ mV s}^{-1}$ . (b) Nyquist plots for rGO@ $\text{Cs}_3\text{PW}_{12}\text{O}_{40}$  and  $\text{Cs}_3\text{PW}_{12}\text{O}_{40}$  as cathodes for lithium ion batteries after second charge/discharge cycle.

34.5  $\Omega$  of  $\text{Cs}_3\text{PW}_{12}\text{O}_{40}$  material used as cathodes for lithium-ion batteries. In the mid to high frequency range, the semicircle radius of  $\text{rGO}@\text{Cs}_3\text{PW}_{12}\text{O}_{40}$  hybrid electrode is smaller than that of pure  $\text{Cs}_3\text{PW}_{12}\text{O}_{40}$  electrode, indicating that the contact resistance and charge transfer impedance of  $\text{rGO}@\text{Cs}_3\text{PW}_{12}\text{O}_{40}$  hybrid electrode are relatively small. This illustrates that the hybrid material prepared by rGO coating  $\text{Cs}_3\text{PW}_{12}\text{O}_{40}$  has excellent conductivity, can promote rapid electron transfer, and improves the electrochemical reaction activity of the cathode material and lithium ions during the insertion/removal process of lithium ions. Thus  $\text{rGO}@\text{Cs}_3\text{PW}_{12}\text{O}_{40}$  hybrid material have excellent battery performance and high charge discharge capacity when used as cathodes for lithium-ion batteries. We further investigated the  $\text{rGO}@\text{Cs}_3\text{PW}_{12}\text{O}_{40}$  cathode cycling to demonstrate the structural stability of 3D  $\text{rGO}@\text{Cs}_3\text{PW}_{12}\text{O}_{40}$  electrodes. SEM image mapping confirms that the morphology of the  $\text{rGO}@\text{Cs}_3\text{PW}_{12}\text{O}_{40}$  electrode remains almost unchanged after 100 cycles of operation at 200  $\text{mA g}^{-1}$  in a coin battery (Figure S1 in supporting information).

To further understand the discharge mechanism of the cathode of the POM-based lithium-ion battery through the x-ray photoelectron spectrum (XPS) before and after the discharge of the  $\text{rGO}@\text{Cs}_3\text{PW}_{12}\text{O}_{40}$  electrode (Figure 6a and 6b). As indicated by Figure 6b, after 20 full-discharge cycles at 1 A/g, we also investigated the W4f XPS spectrum of the  $\text{rGO}@\text{Cs}_3\text{PW}_{12}\text{O}_{40}$  electrode. the  $\text{W}^{6+}$  4f doublet peaks shift toward lower binding energies of 37.2 eV and 35.3 eV, and 34.7 eV and 34.0 eV, corresponding to the  $\text{W}^{5+}$  4f and  $\text{W}^{x+}$  4f ( $x=3, 2, \text{ or } 1$ ) doublet peaks, respectively. This reveals that the  $\text{W}^{6+}$  valence state of Keggin-type  $\text{CsPW}_{12}\text{O}_{40}$  in the electrode is partially reduced to  $\text{W}^{4+}$  and  $\text{W}^{x+}$  ( $x=3, 2, \text{ or } 1$ ) after full discharge. Probably derived from the formation of W–W bond,  $\text{W}^{x+}$  states (like  $\text{W}^{3+}$ ,  $\text{W}^{2+}$ ,  $\text{W}^{1+}$ ) appear between  $\text{W}^{4+}$  and metal  $\text{W}^0$ . Compared to 100% ( $\text{W}^{6+}$ ) in PW<sub>12</sub> structure of  $\text{rGO}@\text{Cs}_3\text{PW}_{12}\text{O}_{40}$  cathode before discharge, the reduction of 15%  $\text{W}^{6+}$  to  $\text{W}^{x+}$  ( $n=1-4$ ) lead to the relative intensities of  $\text{W}^{4+}$  and  $\text{W}^{x+}$  ( $x=3, 2, \text{ or } 1$ ) increase to 10.5% and 5% in the W4f XPS spectrum after initial full discharge to 1.5 V, respectively. Based on the above results, it can infer that the 2 electrons in the cathode material have oxidation-reduction activity, that is, the reduced state  $[\text{PW}_{12}\text{O}_{40}]^{5-}$  the oxidized state  $[\text{PW}_{12}\text{O}_{40}]^{3-}$  undergoes mutual conversion between the gain and loss electrons. The mechanism of  $\text{rGO}@\text{Cs}_3\text{PW}_{12}\text{O}_{40}$  action is shown in Scheme 2.

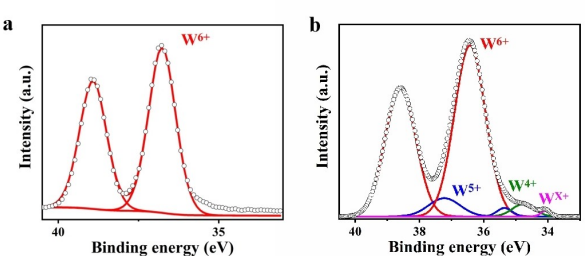
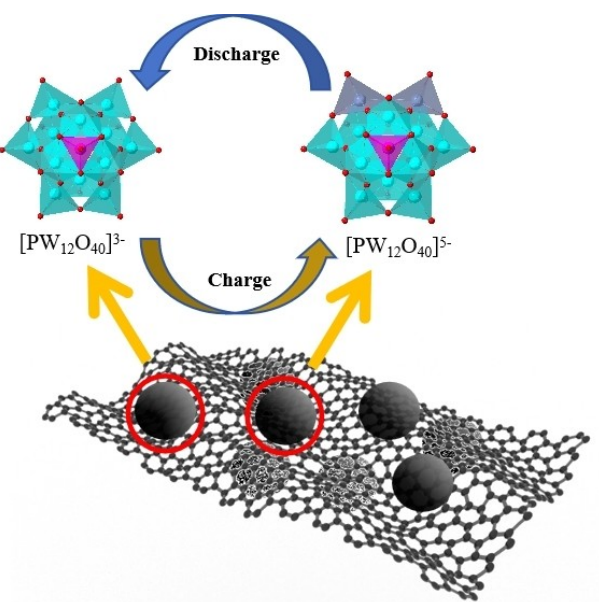


**Figure 6.** W(4f) XPS spectra of the  $\text{rGO}@\text{Cs}_3\text{PW}_{12}\text{O}_{40}$  electrode: (a) before discharge; (b) after 20 full discharge cycles at 1  $\text{A g}^{-1}$ .



**Scheme 2.** Schematic illustration of the proposed charge-discharge mechanism of  $\text{rGO}@\text{Cs}_3\text{PW}_{12}\text{O}_{40}$ -based cathode material in Li-ion battery.

## Conclusions

In summary, a two-step method is used to prepare  $\text{rGO}@\text{Cs}_3\text{PW}_{12}\text{O}_{40}$  hybrid material. Firstly,  $\text{Cs}_3\text{PW}_{12}\text{O}_{40}$  is prepared by ion exchange with phosphotungstic acid and cesium chloride, and then the prepared cesium phosphotungstate is compounded with graphene aqueous solution by hydrothermal method to prepare  $\text{rGO}@\text{Cs}_3\text{PW}_{12}\text{O}_{40}$  hybrid material. Through SEM and TEM testing, it was found that cesium phosphotungstate has a spherical structure with a particle size of 200~600 nm, a smooth surface, and a  $\text{rGO}@\text{Cs}_3\text{PW}_{12}\text{O}_{40}$  hybrid material. Cesium phosphotungstate is uniformly distributed in the graphene layered structure. After structural characterization by FTIR, XRD, TGA, Raman, etc., it was found that our  $\text{rGO}@\text{Cs}_3\text{PW}_{12}\text{O}_{40}$  composite material clearly contains structural characteristic peaks of phosphotungstic acid and graphene, and the content of phosphotungstic acid in the hybrid material is about 54.76%. Finally, we used pure  $\text{Cs}_3\text{PW}_{12}\text{O}_{40}$  and  $\text{rGO}@\text{Cs}_3\text{PW}_{12}\text{O}_{40}$  hybrid material as cathode material for lithium-ion batteries to prepare lithium-ion batteries and tested their electrochemical properties. The  $\text{rGO}@\text{Cs}_3\text{PW}_{12}\text{O}_{40}$  hybrid half-cell exhibits exceptional electrochemical performance, delivering a capacity of approximately 248  $\text{mAh g}^{-1}$  at 50  $\text{mA g}^{-1}$ , excellent rate capability (128  $\text{mAh g}^{-1}$  at 1  $\text{A g}^{-1}$ ), and outstanding cycling stability with a capacity retention of 82%. These results demonstrate the superior performance of POM-based cathodes with long cycling life. The prepared phosphotungstate also effectively inhibits the dissolution of phosphotungstic acid in the electrolyte, significantly enhancing the stability of both charging and discharging cycles, thereby improving battery longevity. This study provides new insights for the design of electrode materials for next-generation lithium-ion batteries.

## Acknowledgements

This work was supported by the National Natural Science Foundation of China (No. 21971221 and 21401162), the Yangzhou University Interdisciplinary Research Foundation for Chemistry Discipline (yzuxk202010), "Qing Lan Project" in Colleges and Universities of Jiangsu Province, Postgraduate Research & Practice Innovation Program of Jiangsu Province (grant number KYCX22\_3467).

## Conflict of Interests

The authors declare no conflict of interest.

## Data Availability Statement

The data that support the findings of this study are available from the corresponding author upon reasonable request.

**Keywords:** batteries • cluster compounds • graphene • polyoxometalates

- [1] M. S. Whittingham, *Chem. Rev.* **2004**, *104*, 4271–4301.
- [2] M. M. Rana, M. Uddin, M. R. Sarkar, S. T. Meraj, G. M. Shafiullah, S. M. Muyeen, M. A. Islam, T. Jamal, *J. Energy Storage* **2023**, *68*, 107811.
- [3] Q. Li, L. Zhang, J. Dai, H. Tang, Q. Li, H. Xue, H. Pang, *Chem. Eng. J.* **2018**, *351*, 441–461.
- [4] M. Jeong, M.-J. Lee, J. Cho, S. Lee, *Adv. Energy Mater.* **2015**, *5*, 1500440.
- [5] X. Zuo, C. Fan, X. Xiao, J. Liu, J. Nana, *ECS Electrochem. Lett.* **2022**, *A50*, 1.
- [6] J. Lee, H. Amari, M. Bahri, Z. Shen, C. Xu, Z. Ruff, C. P. Grey, O. Ersen, A. Aguadero, N. D. Browning, B. L. Mehdi, *Batteries & Supercaps* **2021**, *4*, 1813–1820.
- [7] P. Wang, Z. Wang, P. Wang, A. N. Chishti, H. Zhang, J. Shi, L. Ni, S. Jamil, Y. Wei, *Polyoxometalates* **2024**, *3*, 9140047..
- [8] Q. Shen, C. J. Gómez-García, W. Sun, X. Lai, H. Pang, H. Ma, *Green Chem.* **2021**, *23*, 3104.
- [9] F. Yu, Z. Lang, L. Yin, K. Feng, Y. Xia, H. Tan, H. Zhu, J. Zhong, Z. Kang, Y. Li, *Nat. Commun.* **2020**, *11*, 490.
- [10] L. Ni, J. Gu, J. Jiang, H. Xu, Z. Wu, Y. Wu, Y. Liu, J. Xie, Y. Wei, G. Diao, *Angew. Chem.* **2023**, *135*, e202306528.
- [11] Y. Zhang, J. Liu, S.-L. Li, Z.-M. Su, Y.-Q. Lan, *EnergyChem* **2019**, *1*.
- [12] Y. Fang, Q. Zhang, F. Li, L. Xu, *Chin. J. Chem.* **2021**, *39*, 2315.
- [13] Y. Nishimoto, D. Yokogawa, H. Yoshikawa, K. Awaga, S. Irle, *J. Am. Chem. Soc.* **2014**, *136*, 9042–9052.
- [14] H. Zhang, A. Xie, Y. Shen, L. Qiu, X. Tian, *Phys. Chem. Chem. Phys.* **2012**, *14*, 12757–12763.
- [15] P. Zhu, X. Yang, X. Li, N. Sheng, H. Zhang, G. Zhang, J. Sha, *Dalton Trans.* **2020**, *49*, 79–88.
- [16] H. Wang, S. Hamanaka, Y. Nishimoto, S. Irle, T. Yokoyama, H. Yoshikawa, K. Awaga, *J. Am. Chem. Soc.* **2012**, *134*, 4918–4924.
- [17] K. Wang, Y. Niu, D. Zhao, Y. Zhao, P. Ma, D. Zhang, J. Wang, J. Niu, *Inorg. Chem.* **2017**, *56*, 14053–14059.
- [18] A. Bayaguud, Z. Zhang, M. Geng, Y. Fu, Y. Yu, C. Zhu, *Small Methods* **2019**, *3*, 1900187.
- [19] X. Zhong, Y. Lu, F. Luo, Y. Liu, X. Li, S. Liu, *Chemistry* **2018**, *24*, 3045–3051.
- [20] Y. H. Ding, J. Peng, S. U. Khan, Y. Yuan, *Chemistry* **2017**, *23*, 10338–10343.
- [21] L. Ni, G. Yang, C. Sun, G. Niu, Z. Wu, C. Chen, X. Gong, C. Zhou, G. Zhao, J. Gu, W. Ji, X. Huo, M. Chen, G. Diao, *Mater. Today* **2017**, *6*, 53–64.
- [22] S. Uematsu, Z. Quan, Y. Suganuma, N. Sonoyama, J. *Power Sources* **2012**, *217*, 13–20.
- [23] H. Yoshikawa, C. Kazama, K. Awaga, M. Satoh, J. Wada, *Chem. Commun. (Camb.)* **2007**, 3169–3170.
- [24] R. N. Nasim Khan, N. Mahmood, C. Lv, G. Sima, J. Zhang, J. Hao, Y. Hou, Y. Wei, *RSC Adv.* **2014**, *4*, 7374–7379.
- [25] T. Wei, M. Zhang, P. Wu, Y. J. Tang, S. L. Li, F. C. Shen, X. L. Wang, X. P. Zhou, Y. Q. Lan, *Nano Energy* **2017**, *34*, 205–214.
- [26] W. Deng, Q. Zhang, Y. Wang, *Dalton Trans.* **2012**, *41*, 9817–9831.
- [27] H. Yang, T. Song, L. Liu, A. Devadoss, F. Xia, H. Han, H. Park, W. Sigmund, K. Kwon, U. Paik, *J. Phys. Chem. C* **2013**, *117*, 17376–17381.
- [28] N. Kawasaki, H. Wang, R. Nakanishi, S. Hamanaka, R. Kitaura, H. Shinohara, T. Yokoyama, H. Yoshikawa, K. Awaga, *Angew. Chem. Int. Ed. Engl.* **2011**, *50*, 3471–3474.
- [29] J. J. Chen, M. D. Symes, S. C. Fan, M. S. Zheng, H. N. Miras, Q. F. Dong, L. Cronin, *Adv. Mater.* **2015**, *27*, 4649–4654.
- [30] J. Xie, Y. Zhang, Y. Han, C. Li, *ACS Nano* **2016**, *10*, 5304–5313.
- [31] M. Priyadarshini, S. Shanmugan, K. P. Kirubakaran, A. Thomas, M. Prakash, C. Senthil, C. W. Lee, K. Vediappan, *J. Phys. Chem. Solids* **2020**, *142*, 109468.
- [32] S. Wang, H. Li, S. Li, F. Liu, D. Wu, X. Feng, L. Wu, *Chemistry* **2013**, *19*, 10895–10902.
- [33] K. Kume, N. Kawasaki, H. Wang, T. Yamada, H. Yoshikawa, K. Awaga, *J. Mater. Chem. A* **2014**, *2*, 3801–3807.
- [34] K. Wakamatsu, A. Sekihara, Y. Yamaguchi, R. Matsushima, D. Matsumura, T. Kuila, H. Yoshikawa, *Batteries & Supercaps* **2023**, *6*, e202200385.
- [35] B. Sun, D. Wang, Y. Jiang, R. Wang, L. Lyu, G. Diao, W. Zhang, H. Pang, *Adv. Mater.* **2024**, 2415663.
- [36] D. A. Friesen, J. V. Headley, C. H. Langford, *Environ. Sci. Technol.* **1999**, *33*, 3193–3198.
- [37] K. Li, J. Hu, W. Li, F. Ma, L. Xu, Y. Guo, *J. Mater. Chem.* **2009**, *19*, 8628–8638.
- [38] S. Eigler, C. Dotzer, A. Hirsch, *Carbon* **2012**, *50*, 3666–3673.
- [39] A. A. Ibrahim, D. A. Kospa, O. R. Hayes, A. S. Khder, S. A. El-Hakam, A. I. Ahmed, *RSC Adv.* **2023**, *13*, 15243–15260.
- [40] R. Liu, G. Zhang, H. Cao, S. Zhang, Y. Xie, A. Haider, U. Kortz, B. Chen, N. S. Dalal, Y. Zhao, L. Zhi, C.-X. Wu, L.-K. Yan, Z. Su, B. Keita, *Energy Environ. Sci.* **2016**, *9*, 1012–1023.
- [41] L. M. Malard, M. A. Pimenta, G. Dresselhaus, M. S. Dresselhaus, *Phys. Rep.* **2009**, *473*, 51–87.
- [42] Y.-K. Miura, H. Imai, T. Yokoi, T. Tatsumi, Y. Kamiya, *Microporous Mesoporous Mater.* **2013**, *174*, 34.

Manuscript received: November 8, 2024

Revised manuscript received: December 24, 2024

Accepted manuscript online: December 31, 2024

Version of record online: January 15, 2025